

ZerNet: Convolutional Neural Networks on Arbitrary Surfaces via Zernike Local Tangent Space Estimation

Zhiyu Sun,¹ Jia Lu ² and Stephen Baek¹

Abstract— The research community has observed a massive success of convolutional neural networks (CNN) in visual recognition tasks. Such powerful CNNs, however, do not generalize well to arbitrary-shaped manifold domains. Thus, still many visual recognition problems defined on arbitrary manifolds cannot benefit much from the success of CNNs, if at all. Technical difficulties hindering generalization of CNNs are rooted in the lack of a canonical grid-like representation, the notion of consistent orientation, and a compatible local topology across the domain. Unfortunately, except for a few pioneering works, only very little has been studied in this regard. To this end, in this paper, we propose a novel mathematical formulation to extend CNNs onto two-dimensional (2D) manifold domains. More specifically, we approximate a tensor field defined over a manifold using orthogonal basis functions, called Zernike polynomials, on local tangent spaces. We prove that the convolution of two functions can be represented as a simple dot product between Zernike polynomial coefficients. We also prove that a rotation of a convolution kernel equates to a 2×2 rotation matrix applied to Zernike polynomial coefficients, which can be critical in manifold domains. As such, the key contribution of this work resides in a concise but rigorous mathematical generalization of the CNN building blocks. Furthermore, comparative to the other state-of-the-art methods, our method demonstrates substantially better performance on both classification and regression tasks.

I. INTRODUCTION

The research community has experienced an unprecedented success of CNNs over the last half decade. To this, perhaps, computer vision and (medical) image processing areas have been the biggest contributor as well as beneficiary. It is partly due to the virtue of having a canonical grid-like structure inherently granted on the image domains such that basic operations of CNNs could be defined nicely.

However, in many areas, including even the ones in computer vision, we often face with a visual recognition problem defined on arbitrary-shaped surfaces, or more formally, *manifolds*. For instance, segmentation of a LiDAR scan [26], [11] can be understood as a point-wise classification problem defined on a point-cloud-approximated manifold. Feature detection [35], [15], [28] and correspondence matching [41], [36], [32] on 3D meshes are other typical examples of manifold-based visual recognition problems.

By their nature, most of the manifold-based visual recognition problems are, in fact, not too much different from those in the Euclidean setting. However, in practice, extending CNNs to manifolds is still not quite trivial, mainly due to

¹Z. Sun and S. Baek are with the Department of Industrial and Systems Engineering, the University of Iowa, Iowa City, IA 52242, USA

²J. Lu is with the Department of Mechanical Engineering, the University of Iowa, Iowa City, IA 52242, USA

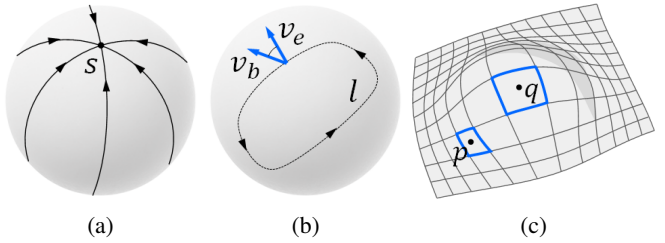


Fig. 1: Problems associated with manifolds when expanding the notion of convolution. (a) a topological sphere cannot have a grid defined on it without a singularity (S); (b) a vector (v_b) parallel-transported along a loop (l) on a manifold might end up in a different orientation (v_e); (c) irregularity of a grid causes varying-size receptive fields.

the geometric and topological constraints. As Bronstein *et al.* [8] points out, “(CNNs) have been most successful on data with an underlying Euclidean or grid-like structure, and in cases where the invariances of these structures are built into networks used to model them.” On manifold domains, however, such a grid-like, tensor-compatible structure may not (and usually do not) exist due to non-planar topology of manifolds. For instance, as widely known via the hairy ball theorem [13], it is impossible to install a grid on a domain homeomorphic to the sphere, without creating at least one singular point, where the notion of orientation breaks off (Figure 1a). Even if there was somehow a grid structure defined nicely without a singularity, the notion of orientation could still be inconsistent across the manifold due to what is known as (non-trivial) holonomy (Figure 1b). This means that sliding convolution kernels along a loop path defined on a manifold may cause an unintended change of orientation when it comes back to the starting point. Moreover, the grid may be irregular most likely, causing varying sizes of effective receptive fields across different locations on the manifold (Figure 1c).

However, despite the benefits of having CNNs defined on manifolds, only very little has been studied yet, except for a few pioneering works by a small community of researchers as we will see in depth in the following section. To this end, in this paper, we propose a new mathematical formulation of CNNs on arbitrary manifolds. The key innovation of the proposed approach resides in the local piece-wise parametrization of a tensor field via the Zernike polynomial bases [40]. These orthogonal basis functions permit a simple but rigorous generalization of convolution via a simple dot product between Zernike polynomial coefficients. Furthermore, a kernel rotation can also be simplified as a

2×2 rotation of the Zernike coefficients, enabling concise definition of angular pooling, which is critical on manifold domains. As such, the greatest benefit of the new formulation is in the fact that it retains mathematical rigor throughout the process of generalization while maintaining simplicity. Finally, building upon the new theoretical foundation, we propose a new approach called Zernike CNNs, or *ZerNets*, and demonstrate an improved performance of our approach in both classification and regression tasks, comparative to the other state-of-the-art methods.

II. RELATED WORKS

In contrast to the explosive amount of other (Euclidean) CNN papers over the last few years, the research community has observed only a limited number of works regarding manifold CNNs so far. Loosely speaking, these works can be categorized into the two following categories.

First are spectral methods [9], [18], [10]. Generally speaking, spectral methods utilize harmonic bases, U , defined on a graph, such as the Laplace-Beltrami spectra [33]. These methods then reparametrize a tensor field x with respect to the harmonic bases, which can be understood as a graph Fourier transform $\mathcal{F}_g(x) = U^T x$. Quite interestingly, the graph convolution operator, $*_g$, can be simplified into the element-wise Hadamard product in the Fourier domain such that $x *_g y = U[(U^T x) \odot (U^T y)]$. As such, convolution of a kernel on a given activation map generalizes quite nicely to graph domains, as demonstrated by Bruna *et al.*[9], [18].

However, these pioneering works suffer from severe computational cost originating from the expensive graph harmonics formulation. Furthermore, convolution kernels in these original works are defined globally over the entire manifold domain rather than locally, such that the true benefit of CNNs—hierarchical assembly of local features—cannot be realized. To this end, Defferrard *et al.*[10] introduced the Chebyshev polynomial approximation to avoid the explicit computation of the graph Laplacian eigenbases. Little later, Kipf *et al.*[22] further improved this strategy by defining more concise convolution kernels based only on the one-ring neighborhoods of the graph. In the meantime, more closely related to surface geometry processing, Boscaini *et al.*[5] introduced the windowed Fourier transform [34] to localize convolution kernels to a local window.

However, despite elegant and mathematically rigorous formulation of the spectral methods, there exist several practical limitations. First of all, even with fast computation strategies, the spectral methods still suffer from a severe computational cost in both preprocessing and inference. This is due to the complexity of computing spectral bases, which essentially is the eigendecomposition of a $n \times n$ matrix, where n is the number of graph nodes. In addition, convolution kernels are implicit in the spectral domain such that the design and implementation of the methods can not be so straightforward. Furthermore, it is not trivial to transfer convolution kernels learned from a certain spectral domain to a different one, especially when the topology of graph is different. Moreover, as well-known in computational geometry, spectral bases

of different manifolds are not guaranteed to be compatible, even if the topology was somehow consistent. On the other hand, spatial approaches are based on a more straightforward, explicit generalization of CNNs [12], [27], [16]. In contrast to the spectral formulations where convolution is implicitly reparametrized via spectral basis functions, in spatial formulations, convolution is defined explicitly on local neighborhoods of graph nodes, quite intuitively expanding the notion defined on pixel-neighborhood in conventional CNNs.

More specifically on surface domains, Masci *et al.*[24] applied convolution kernels on local geodesic disks to achieve manifold convolution. This idea quite naturally generalizes the explicit notion of convolution onto manifold domains. In a similar work, Boscaini *et al.*[6] used anisotropic heat kernels to enable higher expressivity. Monti *et al.*[25] further improved the local geodesic disk convolution idea by introducing the notion of trainable local parametrization such that the coordinate values of the neighboring points on geodesic disks could be learned from data. More recently, Verma *et al.*[38] proposed a more advanced trainable parametrization scheme of the local neighborhood structure by letting the network to learn the correspondence between the kernels. As opposed to the spectral methods, these spatial approaches do not assume global function bases, so that kernels are compatible across different surfaces. In the meantime, however, spatial approaches are heuristics-based such that mathematical rigor is often lost during the spatial discretization process. Furthermore, local neighborhood topology can vary across different locations on the manifold, rendering another obstacle for convolving kernels in a consistent manner.

The new method we propose in this paper combines the advantages of spectral and spatial approaches. In our formulation, the convolution kernels are applied on local tensor fields spatially extracted from each manifold surface, which inherits the compatibility across different surfaces as the key advantage of spatial approaches. In the mean time, the local tensor field is parametrized via an identical set of orthogonal bases (Zernike polynomials), which preserve the mathematical rigor like spectral approaches.

III. ZERNIKE CONVOLUTIONAL NEURAL NETWORKS

In this section, we first introduce Zernike polynomials and their formal definition. We employ them to describe local geometry of a manifold on local tangent spaces. We will then define manifold convolution on the Zernike local tangent spaces and examine their analytic properties. Finally, we discretize the continuous formulation of the Zernike convolution to define Zernike CNNs, or *ZerNets*.

A. Zernike polynomials

Zernike polynomials \hat{Z}_i are a sequence of orthogonal polynomial basis functions defined over the unit disk $\Omega \in \mathbb{R}^2$ such that $\langle \hat{Z}_i, \hat{Z}_j \rangle = \int_{\Omega} \hat{Z}_i(t) \hat{Z}_j(t) dA = 0$ for all $i \neq j$ where $\langle \cdot, \cdot \rangle$ denotes the inner product. The formal definition of the Zernike polynomials is separated into even and odd parts of

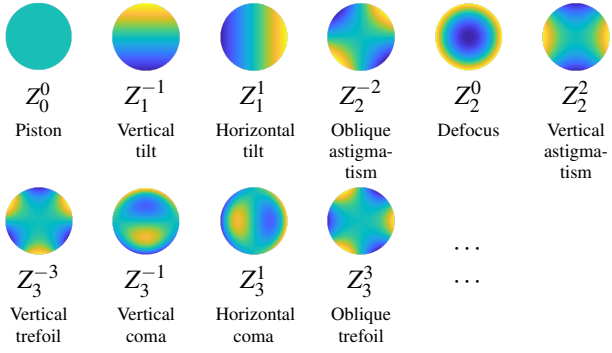


Fig. 2: First few Zernike bases with optical interpretations.

the sequence denoted as $Z_n^m(r, \theta)$ and $Z_n^{-m}(r, \theta)$ respectively:

$$\begin{aligned}\hat{Z}_n^m(r, \theta) &= \hat{R}_n^m(r) \cos(m\theta), \\ \hat{Z}_n^{-m}(r, \theta) &= \hat{R}_n^m(r) \sin(m\theta).\end{aligned}\quad (1)$$

where m and n are non-negative integer indices with $m \leq n$; $r \subseteq [0, 1]$ is the radial distance; and θ is the azimuthal angle on the disk. Here, $\hat{R}_n^m(r)$ is called the Zernike radial polynomial and is defined as:

$$\hat{R}_n^m(r) = \sum_{k=0}^{\frac{n-m}{2}} \frac{(-1)^k (n-k)!}{k! (\frac{n+m}{2} - k)! (\frac{n-m}{2} - k)!} r^{n-2k} \quad (2)$$

for $n-m$ even, and 0 for $n-m$ odd.

Figure 2 illustrates the first few Zernike basis functions. Due to simple analytic properties, Zernike polynomials are widely used in optometry and ophthalmology to describe aberrations of the cornea or to represent lens distortions in optics. As we will see in the later sections, we take the advantage of such simple analytic properties of Zernike polynomial bases for extending CNNs on manifolds.

In practice, Zernike polynomials are normalized with a normalization factor $\sqrt{\frac{2-\delta(m,0)}{\pi}}$ such that the integral over the unit disk becomes unity:

$$Z_n^m(r, \theta) = \hat{Z}_n^m(r, \theta) \sqrt{\frac{2-\delta(m,0)}{\pi}}, \quad (3)$$

where Z_n^m denotes the normalized Zernike polynomial and δ is the Kronecker delta function.

The normalized (orthonormal) Zernike polynomials serve as bases for decomposing a complex function as a weighted sum, such that any function $f(r, \theta)$ defined on the unit disk $[0, 1] \times [0, 2\pi]$ can be expressed as:

$$f(r, \theta) = \sum_{n=0}^{\infty} \sum_{m=-n}^n a_{nm} Z_n^m(r, \theta). \quad (4)$$

where a_{nm} are coefficients or “coordinates” on the Zernike function domain.

B. Zernike convolution

To generalize convolution on an arbitrary differential manifold \mathcal{M} , we introduce functions f and g defined on \mathcal{M} and the involution $\tilde{g}(x) := \overline{g(-x)}$ where $\overline{\cdot}$ denotes the complex

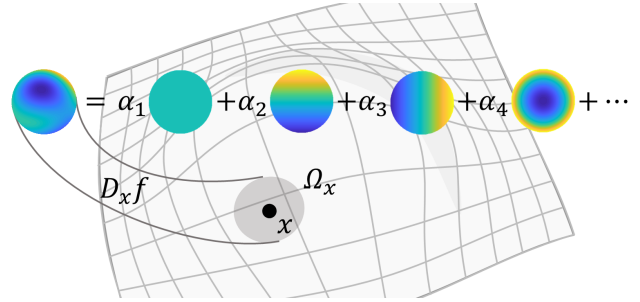


Fig. 3: Zernike decomposition of a function.

conjugate. Then, the convolution of a function f with a function g can be represented as:

$$(f * g)(x) = \int_{\mathcal{M}} f(p) \overline{T_x \tilde{g}(p)} dA = \langle f, T_x \tilde{g} \rangle, \quad (5)$$

where T_x is the parallel transport to x [17, Chapter 1.3]. Here, if the “non-zero” area of \tilde{g} is within a sufficiently small radius, this can further restrict the integral into the local neighborhood $\Omega(x)$ around x :

$$\langle f, T_x \tilde{g} \rangle = \int_{\Omega(x)} f(y) \overline{T_x \tilde{g}(y)} dA. \quad (6)$$

Here, we then estimate the functions f and \tilde{g} on the local tangent space of x using the Zernike function decomposition as in Equation 4:

$$f_x(r, \theta) = \sum_{i=1}^{\infty} \alpha_i Z_i(r, \theta), \quad \overline{\tilde{g}(r, \theta)} = \sum_{i=1}^{\infty} \beta_i Z_i(r, \theta). \quad (7)$$

Here, it should be noted that, for the sake of brevity, we abbreviate the indices of Zernike bases with the index i rather than the full scripts n and m . It should also be noted that after decomposing f and \tilde{g} with respect to the Zernike bases, the integrand $f(p) \overline{T_x \tilde{g}(p)}$ can be written independently of x in a polar coordinates. Therefore, Equation 6 becomes

$$\begin{aligned}\langle f, T_x \tilde{g} \rangle &= \iint_{r, \theta} \sum_i \alpha_i Z_i(r, \theta) \sum_i \beta_i Z_i(r, \theta) r dr d\theta \\ &= \iint_{r, \theta} \sum_{i,j} \alpha_i \beta_j Z_i(r, \theta) Z_j(r, \theta) r dr d\theta \\ &= \sum_{i,j} \alpha_i \beta_j \iint_{r, \theta} Z_i(r, \theta) Z_j(r, \theta) r dr d\theta.\end{aligned}\quad (8)$$

However, from the orthonormality condition, the area integral becomes 1 when $i = j$ and cancels out otherwise. Therefore, we derive the following equation for the Zernike convolution.

$$(f * g)(x) = \sum_{i=1}^{\infty} \alpha_i \beta_i \quad (9)$$

It is worthwhile to remark that it is just a dot product of the Zernike coefficients.

a) *Angle defects*: Our generalization of convolution relies on a parallel transport T_x on a manifold \mathcal{M} . However, on a generalized manifold setting, the parallel transport T_x might still result in difference of orientation due to holonomy of the manifold \mathcal{M} (See Figure 1).

Hence, it could be extremely useful to have a mechanism to compensate the angle defect caused by holonomy. In fact, for instance, Masci *et al.*[24] define an angular pooling operation where a convolution kernel is applied in multiple different orientations and the maximum activation among them is selected.

To enable such kind of operations, we derive a useful rotational property of the Zernike convolution on the local tangent space. To this end, let us consider a Zernike decomposition with an angular displacement t :

$$\begin{aligned} f(r, \theta + t) &= \sum_{\text{even}} a_n^m Z_n^m(r, \theta + t) \\ &+ \sum_{\text{odd}} a_n^{-m} Z_n^{-m}(r, \theta + t) \\ &= \sum_{\text{even}} a_n^m \hat{R}_n^m(r) \cos(m\theta + mt) \\ &+ \sum_{\text{odd}} a_n^{-m} \hat{R}_n^m(r) \sin(m\theta + mt) \end{aligned} \quad (10)$$

Then, from the trigonometric sum and product formulae, we derive

$$\begin{aligned} Z_n^m(r, \theta + t) &= Z_n^{-m}(r, \theta) \cos(mt) + Z_n^m(r, \theta) \sin(mt) \\ Z_n^{-m}(r, \theta + t) &= Z_n^m(r, \theta) \cos(mt) - Z_n^{-m}(r, \theta) \sin(mt) \end{aligned} \quad (11)$$

Therefore, a convolution kernel g after a rotation t can be represented as a simple 2×2 rotational transform of the Zernike coefficients a_n^m and a_n^{-m} . We introduce the term *Zernike angular operator* $\text{Rot}(t)$, such that $\text{Rot}(t)g = T_m a_n^m$ where

$$T_m = \begin{bmatrix} \cos(mt) & -\sin(mt) \\ \sin(mt) & \cos(mt) \end{bmatrix}. \quad (12)$$

Thus, in the Zernike convolution setting, the angular pooling operation can be achieved with any desired angle steps without losing any mathematical rigor, as opposed to the fixed angular bin heuristics as in [24].

b) Patch operator: For the notational convenience, we further introduce *Zernike patch operator*

$$D(x)f = [\alpha_i] = \left[\iint_{r, \theta} f_x(r, \theta) Z_i(r, \theta) r dr d\theta \right], \quad (13)$$

α_i are essentially the Zernike polynomial coefficients approximating a known function f around x , which can be regarded as the extracted intrinsic ‘patch’ on the manifold centered at x . Practically, $D(x)f$ can be evaluated by solving the following system of equations:

$$f_x(r_p, \theta_p) = \sum_{i=1}^n \alpha_i Z_i(r_p, \theta_p) \quad (14)$$

Finally, using the *Zernike patch operator* and *Zernike angular operator*, a concise formulation of manifold convolution in our approach is represented as:

$$(f * g)(x) = \sum_{i=1}^n (\text{Rot}(t)g_i) D_i(x)f, \quad (15)$$

where g denote the filters applied on the extracted ‘patch’ on the manifold, which can be rotated by any arbitrary angular displacement t , n denote a finite number of Zernike functions used for decomposition.

C. ZerNet

Building upon the above definitions, we now define Zernike CNNs, or ZerNets, which are comprised of the following building blocks.

a) Zernike decomposition layer: is a non-trainable layer that interfaces with the input manifold domain. This layer first constructs local patches for each point x on the manifold by approximating the local tensor field around x via finite Zernike decomposition. To achieve so, manifold points are sampled via Poisson disk sampling [30]. Other similar sampling methods can also be employed, as the ZerNet formulation is not very sensitive to sampling. Local patches are then approximated on each point x . The patch boundary is defined by a geodesic disk $B_{r_0}(x)$ centered at each point x with a sufficiently small radius r_0 . We will discuss later, but r_0 is essentially a parameter that determines the receptive fields of convolution kernels, similar to the kernel size— 3×3 , 7×7 , etc.—in plain Euclidean CNNs. Finally, on these local patches, input values defined on the manifold are then decomposed with respect to the Zernike bases $Z_i(r_p, \theta_p)$. This can be done by applying the Zernike patch operator $D(x)$ as in Equation 13.

For implementation, this layer takes an $M \times d$ tensor as an input and outputs an $M \times n \times d$ tensor, where M is the number of total sampled manifold points, n is the number of Zernike bases, and d is the number of channels of the input feature vectors.

b) Zernike convolution layer: takes a tensor field defined on a manifold and outputs an activation tensor field. Each Zernike convolution kernel contains trainable parameters β_i which produces activation based on input tensor patch α_i via Equation 9. In addition, the layer also takes an angular resolution Q as an input. Based on the angular resolution, the convolution kernel is applied in Q different orientations spanning $[0, 2\pi]$ radians. Such orientation-varying convolutions can be done simply by applying 2×2 rotation matrices to Zernike coefficients as in Equations 11 and 12.

Hence, this layer takes an $M \times n \times d$ tensor as input (a manifold activation map outputted from the previous layer) and applies d' kernels with an angular resolution Q . Thus the output shape of this layer is $M \times d' \times Q$.

c) Angular max-pooling layer: is a non-trainable layer to down-sample activation maps defined across different angular resolutions. Similar to the (spatial) max-pooling layers, angular max-pooling layers select the maximum value among activations in different angles.

This layer takes the outputted $M \times d' \times Q$ tensor from the *Zernike convolution layer* as input, outputs a $M \times d'$ tensor which represents the evolved geometric features through the entire convolution operation.

D. Comparison to the other methods

A conventional convolution operation defined on image domains amounts to extracting a local patch of pixels and then taking the weighted sum over a template, or a convolutional filter. The inherent grid-like structure of image domains (i.e. Euclidean) presents a consistent global

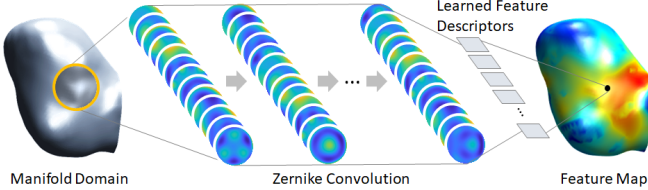


Fig. 4: A schematic overview of a Zernike convolutional neural network.

parametrization property, which allows the application of a template in a consistent orientation across the pixels. In the non-Euclidean setting (manifold), the lack of shift-invariance makes such patch extraction operation position-dependent.

In previous efforts for the generalization of the convolution in the spatial domain on manifolds [24], [7], [25], the patch extraction operation is defined as a re-weighting of the function f at position x by applying a set of weighting functions $w_1(x, \cdot), \dots, w_J(x, \cdot)$ to its neighbors spatially localized around x . In this manner, the local patch can be obtained by mapping from the manifold into some local system of coordinates around x :

$$D_j(x)f = \int_{\chi} w_j(x, x')f(x')dx', j = 1, \dots, J, \quad (16)$$

providing for a intrinsic convolution defined as:

$$(f * g)(x) = \sum_{j=1}^J g_j D_j(x)f, \quad (17)$$

where g denote the filters applied on the extracted patch at position x .

Compared to previous efforts, in the attempt of obtaining a meaningful parametrization at x on manifold, other than adopting an interpolation approach by directly re-weighting its surrounding neighbors, we introduce a decomposition approach by using a sequence of orthogonal bases (Zernike polynomials). Then the intrinsic ‘patch’ extracted via our approach is essentially the Zernike coefficients. For convolution filters, our approach usually comes with a much less required parameters. As for the interpolation approach, the required number of parameters is equal to the number of the weighting functions, which essentially has to be the number of discretized samples in a local patch. Whereas in our case, the ones is the number of the orthogonal bases we chose for the decomposition, which practically can be much smaller. Another deficiency in the previous approaches is the lack of a consistent and meaningful ordering of the applied weighting functions, due to an arbitrary ordering of the local surrounding neighbors in an extracted patch. To this end, the lack of shift-invariance is still not completely addressed while the convolution filter (template) is moving across the manifold. In our formulation, as the ordering of the Zernike coefficients in each extracted ‘patch’ is always consistently corresponding to the set of Zernike polynomials, this issue is no longer existed.

Method	Input	Accuracy
ACNN [7] w/o refinement	SHOT	60.6%
ACNN [7] w/ refinement [29]	SHOT	62.4%
GCNN [24] w/o refinement	SHOT	65.4%
GCNN [24] w/ refinement [29]	SHOT	42.3%
MoNet [25] w/o refinement	SHOT	73.8%
MoNet [25] w/ refinement [39]	SHOT	88.2%
FeaStNet [38] w/o refinement	XYZ	88.1%
FeaStNet [38] w/ refinement [39]	XYZ	92.2%
FeaStNet [38] multi-scale	XYZ	98.7%
ZerNet (Ours) w/o refinement	XYZ	93.9%

TABLE I: Correspondence accuracy on the FAUST human dataset of our method and recent state-of-the-art manifold convolution approaches. Accuracies for the compared methods [24], [7], [25], [38] are directly taken from the corresponding papers.

IV. EXPERIMENTS

We validate the proposed approach against the two major supervised learning tasks, namely, classification and regression. For classification, we tackle a point-wise correspondence matching problem on 3D shapes, which is commonly formalized as a per-vertex classification problem in other state-of-the-art literatures [24], [7], [25], [38]. Regression, on the other hand, is not quite common in the area yet and, thus, we introduce a new benchmark test data set for a per-vertex (scalar-field) regression problem.

A. 3D shape correspondence

The goal of 3D shape correspondence problem is to find semantically meaningful one-to-one matching pair between points on a query surface and points on a reference surface.

a) Dataset: We use the FAUST human dataset [4], following the experimental setup in other state-of-the-art methods [24], [7], [25], [38] we will compare later. The dataset is comprised of 100 watertight meshes of 10 different subjects with 10 different poses for each. Each mesh contains 6,890 vertices and the semantic location of the vertices are consistent across different meshes. Thus, we utilize such pre-established correspondence as ground truth for the training but pretend no such information is provided in testing.

b) Input processing: We choose r_0 equal to approximately 3% of the geodesic diameter of each shape for the local patch extraction. For initial input, we do not rely on a manually-defined feature descriptors such as SHOT descriptor [37] used in [24], [7], [25]. Instead, we take canonical XYZ-coordinates as our model input. The first 21 Zernike polynomial bases are used to approximate the local patches.

c) Architecture: For the fair comparison with the other state-of-the-art methods [24], [7], [25], [38], we adopt Conv128 + Conv256 + Conv512 + FC1200 + FC12000 + Softmax architecture that is most similar to the other methods. The numbers in the layer names indicate the output channel dimensions. Our model was trained using the Adam optimizer [21] with the sparse categorical cross-entropy loss as the objective.

d) Results: To evaluate the performance, we first compare the classification accuracy (*True Classification*)/(*Total*

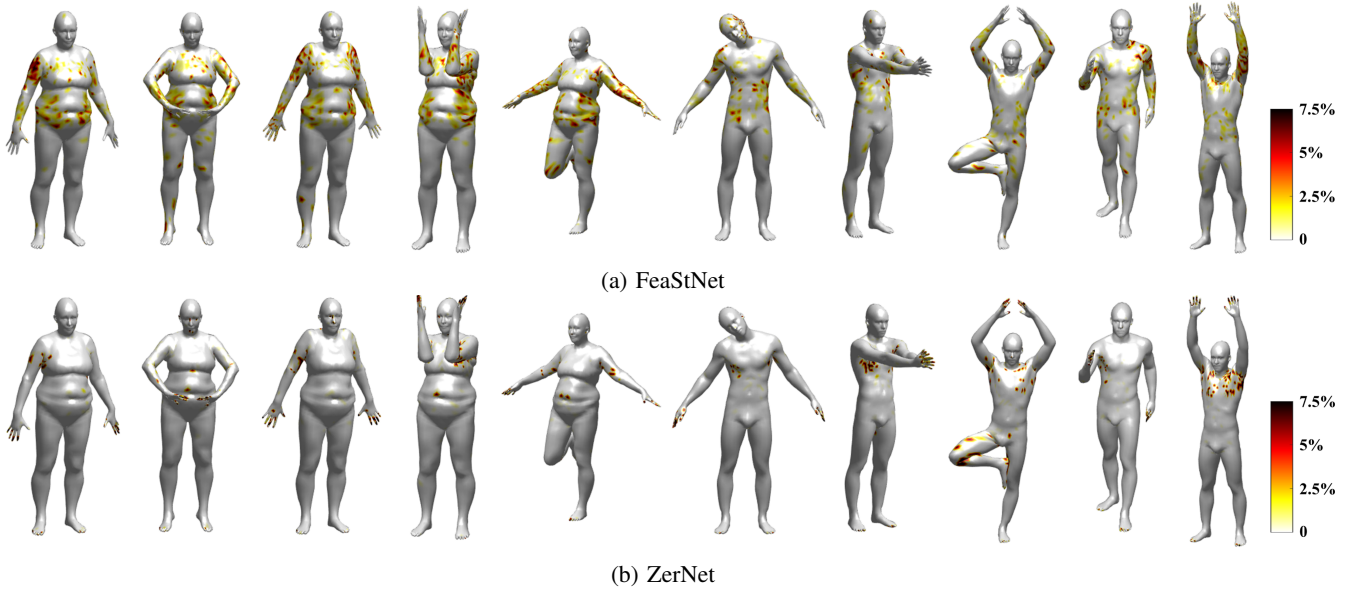


Fig. 5: Point-wise geodesic error (in % of the shape diameter) of ZerNet vs FeaStNet on the FAUST human dataset [4]. Results are generated based on raw performance of both approaches shared a similar single-scale architecture.

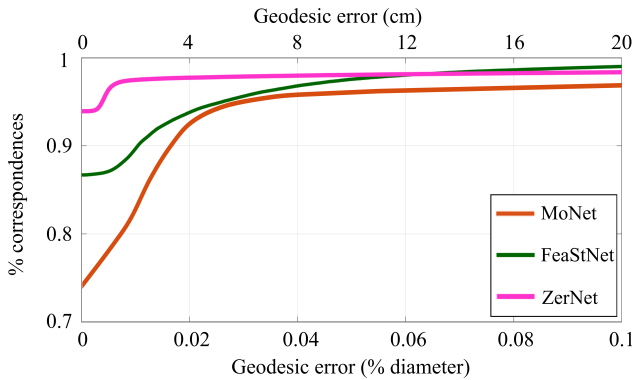


Fig. 6: Shape correspondence quality obtained by different methods on the FAUST human dataset. Results are generated based on the raw performance of each method without additional post-process refinements.

Number of Samples) as reported in Table I. As shown in the table, ZerNet outperforms the other state-of-the-art methods even without additional post-processes for refinement [29], [39]. We note that, in multi-scale with spatial pooling and unpooling, however, FeaStNet [38] shows a better accuracy (98.7%) than ZerNet. However, a fair comparison on this is not available at the current stage of ZerNet development due to the lack of pooling and unpooling operations, which will be our future work.

In addition, we further evaluated the quality of correspondence using the Princeton benchmark [20]. The correspondence quality is measured by the percentage of correctly predicted correspondence within a geodesic disk around the ground-truth point. The results were plotted in Figure 6 with varying radii of the geodesic disk from 0% to 10% of shape diameter.

Figure 5 shows the point-wise geodesic correspondence error of our method; demonstrates a significant improvement over the most recent state-of-the-art method, FeaStNet [38].

B. Scalar field regression

We further validate our method on a regression task. Specifically, the problem is to regress a continuous scalar field defined over a surface using convolutional networks.

a) Dataset: To this end, we introduce a new benchmark dataset for testing scalar field regression on surfaces. The dataset is comprised of 3D surface meshes of 26 cerebral aneurysm cases. The goal is to predict the stress distribution over the membrane surfaces, which is a scalar-field defined on each surface. The ground-truth values come from finite-element analysis (FEA) simulations and are provided along with the data. In contrast to the FAUST dataset, the aneurysm models have different mesh topologies such that the number of vertices and how the vertices are connected are inconsistent across different models.

b) Input processing: Due to the lack of a meaningful shape diameter across the aneurysm models (i.e. as height for human models), we use shape surface area as an reference in this case. The patch radius r_0 is set to make each local patch has an area of approximately 1% of the total mesh surface area. Similar to the shape correspondence case, we use canonical XYZ-coordinates as the input again. Also, the first 21 Zernike polynomial bases are used to approximate the local patches.

c) Architecture: We again use the similar architecture as in the shape correspondence case: Conv128 + Conv512 + Conv1024 + FC800 + FC1. Adam optimizer was used for training, with the mean squared error (MSE) loss as the objective.

d) Result: We cross-validated our method against randomly selected 21 training samples and 5 test samples along

Model ID	ZerNet						FeaStNet					
	MAPE	RRMSE	PCC	HR ₁₀	HR ₂₀	HR ₃₀	MAPE	RRMSE	PCC	HR ₁₀	HR ₂₀	HR ₃₀
TPIa105I	13.13%	15.33%	0.88	58.55%	85.25%	92.25%	16.09%	19.98%	0.80	48.66%	74.37%	86.36%
TPIa166I	10.75%	13.41%	0.85	61.47%	90.07%	95.55%	13.38%	15.86%	0.79	45.72%	79.79%	92.89%
TPIa182I	15.43%	20.69%	0.84	43.62%	75.65%	90.11%	19.99%	24.60%	0.76	35.71%	64.03%	79.27%
TPIa32I	17.45%	18.87%	0.85	50.02%	78.34%	87.86%	23.89%	25.73%	0.65	28.37%	54.48%	73.38%
TPIa33I	9.25%	14.48%	0.89	68.42%	88.86%	96.69%	13.78%	17.71%	0.82	52.25%	78.92%	89.92%

TABLE II: Point-wise regression result of ZerNet vs FeaStNet over five validation data points. Performance was measured with the following criteria: mean absolute percentage error (MAPE), relative root mean square error (RRMSE), Pearson correlation coefficient (PCC) and hit-rate (HR). Subscripts under HR represents the tolerance threshold (10%, 20% and 30%) and HR was calculated as the percentage ratio of the number of the vertices that have the scalar values accurately predicted over the total number of mesh vertices.

with the current state-of-the-art FeaStNet [38]. The result is reported in Table II. In addition, Figure 7 displays the prediction result of the regression models on the five validation cases. On test samples, ZerNet outperformed FeaStNet for all metrics.

It should be noted that both ZerNet and FeaStNet fails to predict correct values near the boundary of the surfaces. This may be due to incorrect boundary conditions (“zero-padding” is enforced currently). Hence, it would be worthwhile to investigate more sophisticated boundary conditions such as the Neumann condition for future research.

V. CONCLUSION

In this paper, we introduced a new concept of Zernike convolution as a way to generalize conventional convolution onto manifold domains. We showed that Zernike convolution seamlessly generalizes convolution operations on arbitrary manifolds in a mathematically rigorous but concise manner. In particular, we proved that manifold convolution could be nicely formalized through decomposition of local patches using Zernike basis functions and that convolution operations became simple dot products of Zernike polynomial coefficients. In addition, we showed that angular pooling, which could be critical in manifold settings, could also be rigorously represented as a simple 2×2 rotation. Building upon this, we demonstrated that ZerNets outperform other state-of-the-art methods on both classification and regression tasks.

For the future work, it would be worth exploring ways to further equip ZerNets with the other essential building blocks of CNNs such as pooling/unpooling, transposed convolution, boundary padding, and varying convolution sizes and strides. Particularly, encoder-decoder type networks on manifolds would be an interesting direction of research, as it can benefit potentially a large amount of computational geometry applications that requires parametrization (i.e. latent space embedding) of geometric shapes (e.g. [1], [19], [14], [3], [23], [2], [31]).

REFERENCES

- [1] S.-Y. Baek and K. Lee. Parametric human body shape modeling framework for human-centered product design. *Computer-Aided Design*, 44(1):56–67, 1 2012.
- [2] S.-Y. Baek and K. Lee. Statistical foot-shape analysis for mass-customisation of footwear. *International Journal of Computer Aided Engineering and Technology*, 8(1/2):80–98, 1 2016.
- [3] S.-Y. Baek, J. H. Wang, I. Song, K. Lee, J. Lee, and S. Koo. Automated bone landmarks prediction on the femur using anatomical deformation technique. *Computer-Aided Design*, 45(2):505–510, 2 2013.
- [4] F. Bogo, J. Romero, M. Loper, and M. J. Black. FAUST: Dataset and evaluation for 3D mesh registration. In *Proceedings IEEE Conf. on Computer Vision and Pattern Recognition (CVPR)*, Piscataway, NJ, USA, June 2014. IEEE.
- [5] D. Boscaini, J. Masci, S. Melzi, M. M. Bronstein, U. Castellani, and P. Vandergheynst. Learning class-specific descriptors for deformable shapes using localized spectral convolutional networks. In *Computer Graphics Forum*, volume 34, pages 13–23. Wiley Online Library, 2015.
- [6] D. Boscaini, J. Masci, E. Rodolà, and M. Bronstein. Learning shape correspondence with anisotropic convolutional neural networks. In *Advances in Neural Information Processing Systems*, pages 3189–3197, 2016.
- [7] D. Boscaini, J. Masci, E. Rodolà, M. M. Bronstein, and D. Cremers. Anisotropic diffusion descriptors. In *Computer Graphics Forum*, volume 35, pages 431–441. Wiley Online Library, 2016.
- [8] M. M. Bronstein, J. Bruna, Y. LeCun, A. Szlam, and P. Vandergheynst. Geometric deep learning: going beyond euclidean data. *IEEE Signal Processing Magazine*, 34(4):18–42, 2017.
- [9] J. Bruna, W. Zaremba, A. Szlam, and Y. LeCun. Spectral networks and locally connected networks on graphs. *arXiv preprint arXiv:1312.6203*, 2013.
- [10] M. Defferrard, X. Bresson, and P. Vandergheynst. Convolutional neural networks on graphs with fast localized spectral filtering. In *Advances in Neural Information Processing Systems*, pages 3844–3852, 2016.
- [11] B. Douillard, J. Underwood, N. Kuntz, V. Vlaskine, A. Quadros, P. Morton, and A. Frenkel. On the segmentation of 3d lidar point clouds. In *Robotics and Automation (ICRA), 2011 IEEE International Conference on*, pages 2798–2805. IEEE, 2011.
- [12] D. K. Duvenaud, D. Maclaurin, J. Iparragirre, R. Bombarell, T. Hirzel, A. Aspuru-Guzik, and R. P. Adams. Convolutional networks on graphs for learning molecular fingerprints. In *Advances in neural information processing systems*, pages 2224–2232, 2015.
- [13] M. Eisenberg and R. Guy. A proof of the hairy ball theorem. *The American Mathematical Monthly*, 86(7):571–574, 1979.
- [14] O. Freifeld and M. J. Black. Lie bodies: A manifold representation of 3D human shape. In *European Conf. on Computer Vision (ECCV)*, Part I, LNCS 7572, pages 1–14. Springer-Verlag, Oct. 2012.
- [15] R. Harik, Y. Shi, and S. Baek. Shape terra: mechanical feature recognition based on a persistent heat signature. *Computer-Aided Design and Applications*, 14(2):206–218, 2017.
- [16] Y. Hechtlinger, P. Chakravarti, and J. Qin. A generalization of convolutional neural networks to graph-structured data. *arXiv preprint arXiv:1704.08165*, 2017.
- [17] C. Heil. *Introduction to Harmonic Analysis*. Applied and Numerical Harmonic Analysis. Birkhäuser Boston, 2008.
- [18] M. Henaff, J. Bruna, and Y. LeCun. Deep convolutional networks on graph-structured data. *arXiv preprint arXiv:1506.05163*, 2015.
- [19] K. kai Shen, J. Fripp, F. Mriauudeau, G. Chtelat, O. Salvado, and P. Bourgeat. Detecting global and local hippocampal shape changes in alzheimer’s disease using statistical shape models. *NeuroImage*, 59(3):2155 – 2166, 2012.
- [20] V. G. Kim, Y. Lipman, and T. Funkhouser. Blended intrinsic maps. In *ACM Transactions on Graphics (TOG)*, volume 30, page 79. ACM, 2011.
- [21] D. P. Kingma and J. Ba. Adam: A method for stochastic optimization. *CoRR*, abs/1412.6980, 2014.
- [22] T. N. Kipf and M. Welling. Semi-supervised classification with graph convolutional networks. *arXiv preprint arXiv:1609.02907*, 2016.

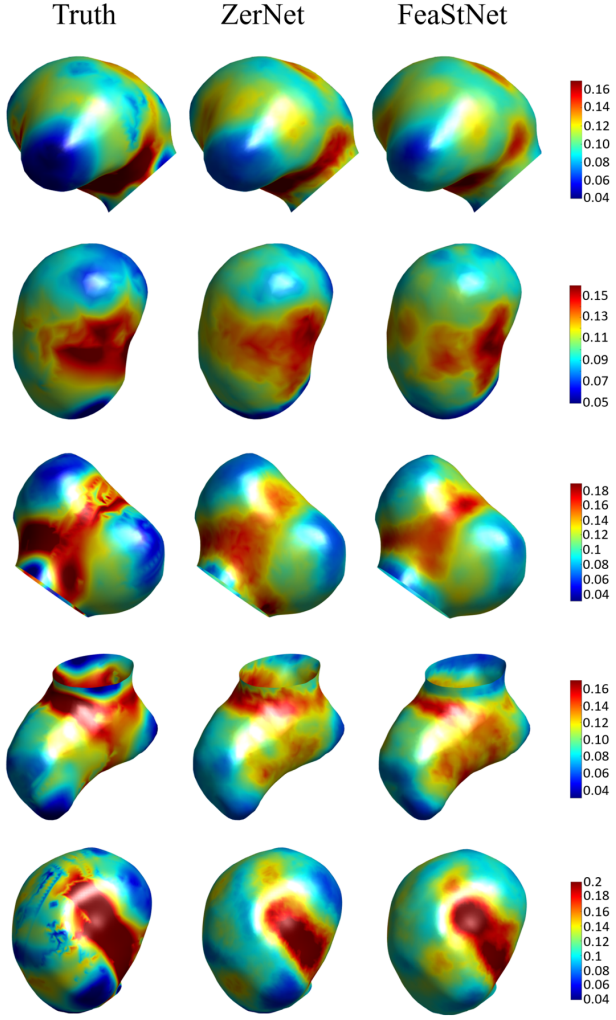


Fig. 7: Visualization of the estimated wall stress distribution on five test data. Each row corresponds to the row of the same order in Table II.

- [23] M. Loper, N. Mahmood, J. Romero, G. Pons-Moll, and M. J. Black. SMPL: A skinned multi-person linear model. *ACM Trans. Graphics (Proc. SIGGRAPH Asia)*, 34(6):248:1–248:16, Oct. 2015.
- [24] J. Masci, D. Boscaini, M. Bronstein, and P. Vandergheynst. Geodesic convolutional neural networks on riemannian manifolds. In *Proceedings of the IEEE international conference on computer vision workshops*, pages 37–45, 2015.
- [25] F. Monti, D. Boscaini, J. Masci, E. Rodola, J. Svoboda, and M. M. Bronstein. Geometric deep learning on graphs and manifolds using mixture model cnns. In *Proc. CVPR*, volume 1, page 3, 2017.
- [26] F. Moosmann, O. Pink, and C. Stiller. Segmentation of 3d lidar data in non-flat urban environments using a local convexity criterion. In *Intelligent Vehicles Symposium, 2009 IEEE*, pages 215–220. IEEE, 2009.
- [27] M. Niepert, M. Ahmed, and K. Kutzkov. Learning convolutional neural networks for graphs. In *International conference on machine learning*, pages 2014–2023, 2016.
- [28] A. Nurunnabi, G. West, and D. Belton. Outlier detection and robust normal-curvature estimation in mobile laser scanning 3d point cloud data. *Pattern Recognition*, 48(4):1404–1419, 2015.
- [29] M. Ovsjanikov, M. Ben-Chen, J. Solomon, A. Butscher, and L. Guibas. Functional maps: A flexible representation of maps between shapes. *ACM Trans. Graph.*, 31(4):30:1–30:11, July 2012.
- [30] J.-L. Peyrot, F. Payan, and M. Antonini. Feature-preserving direct blue noise sampling for surface meshes. In *Eurographics (Short Papers)*, pages 9–12, 2013.

- [31] L. Pishchulin, S. Wuhrer, T. Helten, C. Theobalt, and B. Schiele. Building statistical shape spaces for 3d human modeling. *Pattern Recognition*, 67:276–286, 2017.
- [32] E. Rodolà, S. Rota Bulo, T. Windheuser, M. Vestner, and D. Cremers. Dense non-rigid shape correspondence using random forests. In *Proceedings of the IEEE Conference on Computer Vision and Pattern Recognition*, pages 4177–4184, 2014.
- [33] S. Rosenberg. *The Laplacian on a Riemannian manifold: an introduction to analysis on manifolds*. Number 31. Cambridge University Press, 1997.
- [34] D. I. Shuman, B. Ricaud, and P. Vandergheynst. Vertex-frequency analysis on graphs. *Applied and Computational Harmonic Analysis*, 40(2):260–291, 2016.
- [35] S. Song and J. Xiao. Sliding shapes for 3d object detection in depth images. In *European conference on computer vision*, pages 634–651. Springer, 2014.
- [36] Z. Sun, Y. He, A. Gritsenko, A. Lendasse, and S. Baek. Deep spectral descriptors: Learning the point-wise correspondence metric via Siamese deep neural networks. *arXiv Preprint: arXiv:1710.06368*, 10 2017.
- [37] F. Tombari, S. Salti, and L. Di Stefano. Unique signatures of histograms for local surface description. In *European conference on computer vision*, pages 356–369. Springer, 2010.
- [38] N. Verma, E. Boyer, and J. Verbeek. Feastnet: Feature-steered graph convolutions for 3d shape analysis. In *CVPR 2018-IEEE Conference on Computer Vision & Pattern Recognition*, 2018.
- [39] M. Vestner, R. Litman, E. Rodolà, A. M. Bronstein, and D. Cremers. Product manifold filter: Non-rigid shape correspondence via kernel density estimation in the product space. In *CVPR*, pages 6681–6690, 2017.
- [40] Z. von F. Beugungstheorie des schneidenverfahrens und seiner verbesserten form, der phasenkontrastmethode. *Physica*, 1(7-12):689–704, 1934.
- [41] A. Zaharescu, E. Boyer, K. Varanasi, and R. Horaud. Surface feature detection and description with applications to mesh matching. In *2009 IEEE Conference on Computer Vision and Pattern Recognition*, pages 373–380, June 2009.